GEOCHEMISTRY

# Volcanic $CO_2$ degassing postdates thermogenic carbon emission during the end-Permian mass extinction

**Yuyang Wu[1,2†], Ying Cui[2*†], Daoliang Chu[1*], Haijun Song[1], Jinnan Tong[1], Jacopo Dal Corso[1], Andy Ridgwell[3]**



**Massive carbon dioxide ($CO_2$) emissions are widely assumed to be the driver of the end-Permian mass extinction (EPME). However, the rate of and total $CO_2$ released, and whether the source changes with time, remain poorly understood, leaving a key question surrounding the trigger for the EPME unanswered. Here, we assimilate reconstructions of atmospheric $P_{CO_2}$ and carbonate $\delta^{13}C$ in an Earth system model to unravel the history of carbon emissions and sources across the EPME. We infer a transition from a $CO_2$ source with a thermogenic carbon isotopic signature associated with a slower emission rate to a heavier, more mantle-dominated volcanic source with an increased rate of emissions. This implies that the $CO_2$ degassing style changed as the Siberian Traps emplacement evolved, which is consistent with geochemical proxy records. Carbon cycle feedbacks from terrestrial ecosystem disturbances may have further amplified the warming and the severity of marine extinctions.**

## INTRODUCTION

The end-Permian mass extinction [EPME, ~252 million years (Ma)] is characterized by the occurrence of extreme global warming of 7° to >10°C (*1*–*6*) and was accompanied by a marked perturbation of the global carbon cycle, as indicated by a negative carbon isotope excursion (CIE) (*7*, *8*) as well as proxy evidence for elevated atmospheric $P_{CO_2}$ (partial pressure of $CO_2$) (*9*–*11*) and reduced ocean pH (*12*, *13*). The trigger for the event and source of the $^{13}C$-depleted carbon, at least of the initial $CO_2$ release to the atmosphere, is generally ascribed to the Siberian Traps Large Igneous Province (LIP), with possible contributions from felsic volcanism along the circum-Pangea subduction zone (*14*–*16*). However, in previous studies reconstructing $CO_2$ emission rates, the carbon isotopic values of the carbon source ($\delta^{13}C_{source}$) were assumed to be constant across the event (*17*, *18*) or just two potential isotopically distinct end-member inputs were considered with a rapid switch between them (*12*, *13*). For instance, using a carbon cycle box model to match observed $\delta^{13}C$ and surface ocean pH ($\delta^{11}B$) trends, Jurikova *et al.* (*13*) inferred an initially slow release of $^{13}C$-enriched mantle $CO_2$ (−6‰) that predated the rapid release of $^{13}C$-depleted carbon emission (−18‰). In contrast, Clarkson *et al.* (*12*) came to an opposite model-based conclusion, with a slow emission of $CO_2$ ($\delta^{13}C_{source}$ < −12.5‰) followed by faster rate of emissions (2.4 Pg C year$^{-1}$ over 10,000 years) with a $\delta^{13}C_{source}$ value near 0‰. To address this uncertainty, we simultaneously invert (assimilate) in an Earth system model stacked carbon isotopes from marine carbonates and published $P_{CO_2}$ records to elucidate how the source of emitted $CO_2$ varied across the EPME. In diagnosing continuously evolving emissions and carbon sources across the EPME, we can also help constrain the role of carbon-climate feedbacks, which likely varied in strength with time (*19*).

[1]State Key Laboratory of Biogeology and Environmental Geology, School of Earth Sciences, China University of Geosciences, Wuhan 430074, China. [2]Department of Earth and Environmental Studies, Montclair State University, Montclair, NJ 07043, USA. [3]Department of Earth Sciences, University of California Riverside, Riverside, CA 92521, USA.
*Corresponding author. Email: cuiy@montclair.edu (Y.C.); chudl@cug.edu.cn (D.C.)
†These authors contributed equally to this work.

## RESULTS AND DISCUSSION

### Degassing style change based on $\delta^{13}C$-$P_{CO_2}$ "double inversion"

Previous carbon cycle modeling studies on the EPME mostly adopted a forward box modeling approach (*12*, *13*, *20*–*24*). The few published inverse modeling studies, in which continuously varying carbon emissions were diagnosed, were based on a carbon isotope assimilation approach, targeting $\delta^{13}C$ signal of marine dissolved inorganic carbon (DIC) inferred from a single site of either marine carbonates (*17*) or marine algae biomarker based on short-chain *n*-alkanes (*18*). However, this approach is only capable of generating a nonunique carbon emission solution that is dependent on the assumed $\delta^{13}C_{source}$, which is further considered to be invariant, precluding understanding of whether and how the $\delta^{13}C_{source}$ values evolve with changes in degassing styles of the volcanism. In contrast, simultaneously assimilating paired $\delta^{13}C$ and $P_{CO_2}$ (or ocean pH) records in a model provides two independent constraints, which allows for the computation (inversion) of a time-varying $\delta^{13}C_{source}$ reflecting the $CO_2$ degassing style. To date, such double-inversion experiments have only been applied to unravel carbon emission history during the Paleocene-Eocene Thermal Maximum (*25*) and Cretaceous oceanic anoxic event 1a (*26*).

To elucidate how $\delta^{13}C_{source}$ may have evolved through time across the EPME, we use a stacked marine carbonate $\delta^{13}C$ ($\delta^{13}C_{carb}$) record together with a previously published, near-continuous $P_{CO_2}$ record (*9*), with both placed on a well-constrained geochronology based on conodont biostratigraphy (*27*, *28*) and radiometric dating (*29*). High-resolution biostratigraphy based on seven conodont biozones (Fig. 1), high-precision $^{206}Pb/^{238}U$ dating (*29*), and similar CIE profiles in both marine and terrestrial $\delta^{13}C$ records (*9*) allow for the alignment between the global $\delta^{13}C_{carb}$ and $P_{CO_2}$ with quantifiable uncertainty that ranges from 31 to 37 thousand years (ka) (see age alignment sensitivity analyses in the Supplementary Materials). We use these as inputs to the cGENIE Earth system model configured in a data inversion mode [e.g., (*25*) and see Materials and Methods for detailed model descriptions] and use $\delta^{11}B$-based pH proxy data subsequently as a test of

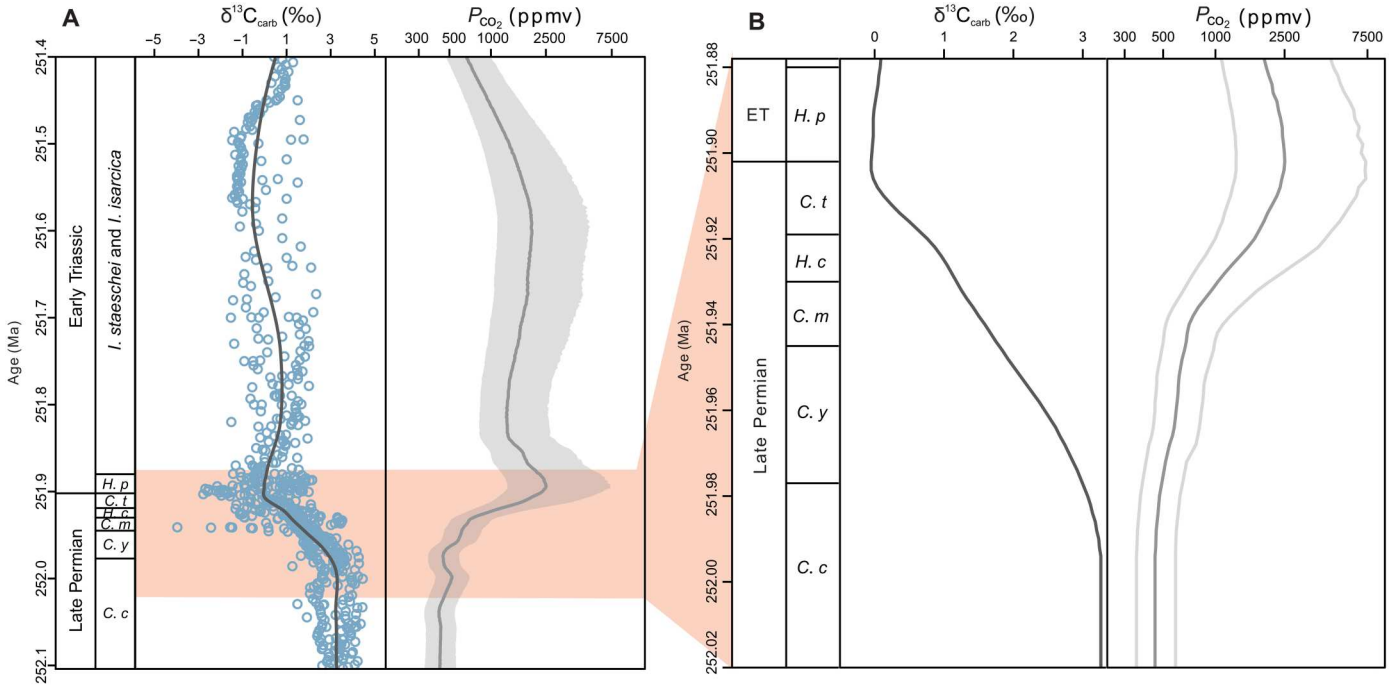


**Fig. 1. Two data assimilation constraints used in the double-inversion experiments using cGENIE Earth system model.** (**A**) Stacked carbonate $\delta^{13}C_{carb}$ and continuous $P_{CO_2}$ records (on a log scale) estimated from $C_3$ land plant $\delta^{13}C$ in southwestern China during the EPME (*9*). (**B**) Stacked carbonate $\delta^{13}C$ across the study interval. For two data assimilation constraints, the LOESS fit curve of $\delta^{13}C_{carb}$ and the 16th percentiles, median, and 84th percentiles of the continuous $P_{CO_2}$ records from (*9*) representing three kinds of $CO_2$ scenarios are applied in the double-inversion experiments. The conodont zones (*27*, *28*) and radiometric ages (*29*) are from the GSSP Meishan section. ET, Early Triassic; *C. c*, *Clarkina changxingensis*; *C. y*, *Clarkina yini*; *C. m*, *Clarkina meishanensis*; *H. c*, *Hindeodus changxingensis*; *C. t*, *Clarkina taylorae*; *H. p*, *Hindeodus parvus*; *I.*, *Isarcicella*.

the derived scenarios. Our chosen records of $\delta^{13}C_{carb}$ and $P_{CO_2}$ have several advantages for constraining the carbon emission history during the EPME: (i) The use of a $\delta^{13}C_{carb}$ stack rather than a single $\delta^{13}C$ profile of marine carbonate or algae biomarker (*18*) helps exclude minor fluctuations caused by local effects and/or sparse sampling in a single record; (ii) the high-resolution $P_{CO_2}$ record estimated by carbon isotope fractionation of $C_3$ land plants from southwestern China is near continuous and has already been aligned with the $\delta^{13}C_{carb}$ forcing (*9*); and (iii) the near-continuous $P_{CO_2}$ record has a higher temporal resolution than the available pH datasets (*12*, *13*) or phytane-based $P_{CO_2}$ estimates (*11*, *30*), enabling the potential to offer previously unidentified insight into the evolving carbon emissions across the EPME.

In our model simulations, we assimilate data spanning the end-Permian CIE across the first pulse of marine extinction (i.e., 251.941 ± 0.037 Ma). The CIE is defined by a rapid decline in $\delta^{13}C_{carb}$ from 3.3‰ at 251.994 Ma to a nadir of −0.1‰ at 251.902 Ma (Fig. 1) and has a duration of ~92 ka based on $^{206}Pb/^{238}U$ dating (*29*) and conodont biostratigraphy (*27*, *28*) (see data file S2 for age correlation and conodont biozones); hence, this interval of simulation is focused on in our analysis. We explore uncertainty in the reconstructed atmospheric $CO_2$ curve, as well as CIE magnitude and duration, through an ensemble of 23 different model experiments (detailed model experiments are described in Materials and Methods and tables S1 and S2) but focus on the results of a single model experiment taking the median $P_{CO_2}$ estimate from Wu *et al.* (*9*) as input. This median $CO_2$ scenario is characterized by a peak value of ~2500 parts per million by volume (ppmv) (experiment 2 in table S1), consistent with independent proxy estimates based on stomata index, paleosol carbonates, and phytanes that also show similar peak values of ~2100 to ~2600 ppmv across the EPME (*10*, *11*, *31*).

Regardless of the model assumptions, we find that carbon emissions during the CIE are characterized by a change of degassing style that, while continually varying, can be divided into two distinct phases (i.e., phase 1 and phase 2) with characteristic $\delta^{13}C_{source}$ values and rates (Fig. 2, figs. S1 and S3, table S1, and data file S1). In our standard median $CO_2$ scenario experiment, the $\delta^{13}C_{source}$ value characterizing emissions during phase 1 (from 251.994 to 251.942 Ma) is lower (average ~ −16‰; peak ~ −30‰) than that for phase 2 (from 251.942 to 251.902 Ma; average ~ −9‰; peak ~ −14‰). Associated with this, the diagnosed carbon emission rate during phase 1 (~0.2 Pg C $year^{-1}$) is ~3.5 times slower than that during phase 2 (~0.7 Pg C $year^{-1}$). As a result, the corresponding cumulative carbon emissions associated with the two phases are 5000 and 21,000 Pg C, respectively. This diagnosed degassing style change suggests a transition of $CO_2$ source during the emplacement of Siberian Traps volcanism in which sill intrusions into organic-rich sediments dominated phase 1, followed by an interval of more mantle $CO_2$ dominated outgassing (phase 2). In our diagnosed scenario, thermogenic carbon [−25 to −40‰; (*32*)] would have been mixed and diluted with volcanic $CO_2$ (ca. −6‰) and released relatively slowly over ~50 ka, driving the initial 1.7‰ negative CIE and increasing $P_{CO_2}$ from ~450 to ~750 ppmv during phase 1. Extrusive magmatism then gradually comes to dominate phase 2, with emission rates increasing and the degassed $CO_2$ converging

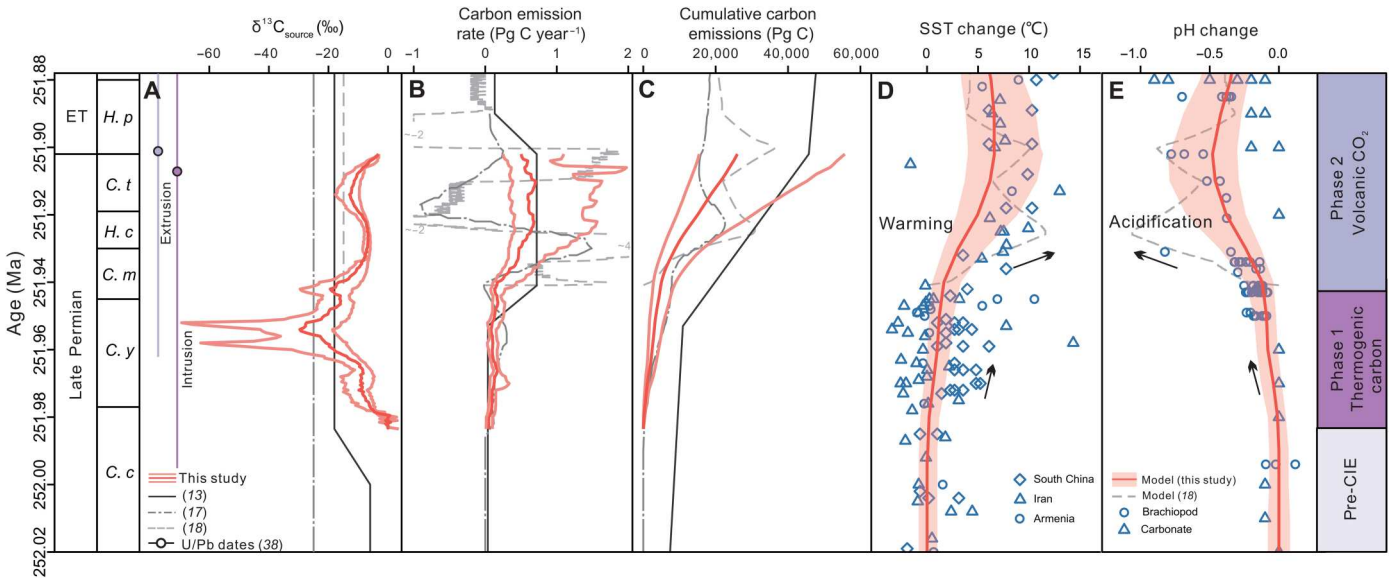


**Fig. 2. The modeled time-varying carbon emissions and model-data comparisons of changes in SST and pH.** (**A**) Modeled time-varying $\delta^{13}C_{source}$ of three standard experiments (experiments 1 to 3 in table S1) during the CIE divided into phase 1 (dominated by thermogenic carbon emissions) and phase 2 with mantle $CO_2$-dominated carbon emissions. Two $^{206}Pb/^{238}U$ ages of 251.907 ± 0.067 Ma characterized by sill intrusion and 251.901 ± 0.061 Ma marked by extrusive pyroclastic rocks are shown here (*38*). (**B**) Diagnosed rates of two-phase carbon emissions (1 Pg = $10^{15}$ g) compared with previously published modeling results (*13*, *17*, *18*). (**C**) Modeled cumulative amount of carbon emissions during the CIE compared with published model estimates (*13*, *17*, *18*). (**D**) Modeled changes in tropical (10°S to 10°N) SST (median value and lower and upper estimates are from three standard runs: experiments 1 to 3 in table S1) and comparison to low-latitude proxy SST change calculated based on conodont $\delta^{18}O$ from South China (*1*–*3*), Iran (*36*), and Armenia (*4*). (**E**) Modeled surface oceanic pH change (median value and lower and upper estimates are from three standard runs: experiments 1 to 3 in table S1) and comparison to proxy pH records based on boron isotopes of brachiopod from northern Italy and South China (*13*), and boron isotopes of marine carbonates from United Arab Emirates (*12*).

toward a more volcanic end-member (−6‰). This second phase change in degassing style drove a further ~1.6‰ decrease in $\delta^{13}C_{carb}$, but with atmospheric $P_{CO_2}$ now rising much more sharply (from 750 to ~2500 ppmv). However, it should be noted that thermogenic releases did not necessarily cease during phase 2, because the average $\delta^{13}C_{source}$ value is −9‰ for phase 2 (e.g., minimum $\delta^{13}C_{source}$ value is −14‰ in median $P_{CO_2}$ scenario), which is better interpreted as a mixed volcanic and thermogenic carbon source rather than a sole volcanic $CO_2$ end-member.

Sensitivity tests using different $P_{CO_2}$ forcings, CIE magnitudes, CIE durations, and alignment scenarios of maximum $P_{CO_2}$ versus minimum $\delta^{13}C_{carb}$ further support the source of $CO_2$ transition from a relatively small amount of thermogenic $CO_2$ to large quantities of primarily volcanic $CO_2$ (Fig. 2A, figs. S1 to S3, and tables S1 and S2). For example, sensitivity tests of $P_{CO_2}$ forcing show that the "high" $CO_2$ scenario is associated with higher peak $\delta^{13}C_{source}$ values of −19 and −10‰ during the two phases, whereas the "low" $CO_2$ scenario is linked to lower peak $\delta^{13}C_{source}$ values of −69 and −18‰ during the two phases (Fig. 2A and table S1). In addition, a larger CIE magnitude, shorter CIE duration, and accounting for temporal uncertainty associated with the timing of the $CO_2$ maximum versus the $\delta^{13}C_{carb}$ minimum suggest that $\delta^{13}C_{source}$ could be even lower during phase 1 (<−30‰), but the two-phase emission patterns remain robust (see the Supplementary Materials for sensitivity analyses).

Previously proposed carbon sources include biogenic methane [$\delta^{13}C_{source} \approx -60$‰; (*20*)], thermogenic methane (and/or $CO_2$) from thermal metamorphism or rapid oxidation of organic-rich rock [$\delta^{13}C_{source} \approx -25$ to −45‰; (*23*)], and volcanic $CO_2$ [$\delta^{13}C_{source} \approx -6$‰; (*24*)] or a combination of various sources [e.g., (*12*, *13*, *18*)]. Our modeled average $\delta^{13}C_{source}$ value of −13‰ (−19 to −9‰) across the two phases falls within the range of values previously reported based on calcium isotope box model [$\delta^{13}C_{source} = -15$‰; (*33*)], biogeochemical box model [$\delta^{13}C_{source} = -6$ and −18‰; (*13*)], and $\delta^{13}C$ inversions [$\delta^{13}C_{source} = -15$‰; (*18*)] (see table S3 for the detailed summary). These estimates imply a combination of volcanic $CO_2$ with thermogenic $CO_2$ and/or organic matter oxidation, but allowing for a small contribution from much more $^{13}C$-depleted sources such as biogenic methane. For instance, in our median $P_{CO_2}$ scenario, the average $\delta^{13}C_{source}$ value is −13‰, which implies ~20% contribution of thermogenic $CO_2$ (−25‰), ~75% contribution of volcanic $CO_2$ (−6‰) and ~5% biogenic methane (-60‰). It is also possible that terrestrial and/or marine organic carbon cycle feedbacks provide a form of $^{13}C$-depleted end-member (*34*).

## Evidence for changes in degassing style

The occurrence of thermogenic carbon emissions before the major release of volcanic $CO_2$ during the EPME is consistent with rising sea surface temperatures (SSTs) (Figs. 2, D and E, and 3 and data file S1 and S2). The reconstructed SSTs from the Global Boundary Stratotype Section and Point (GSSP) Meishan section using conodont oxygen isotopes in low latitudes show two episodes of warming, with a temperature rise of 3° and 6°C, respectively (1, 3), and corresponding to the two $CO_2$ emission phases (conodont *Clarkina yini* zone in phase 1 and from *Clarkina meishanensis* to *Hindeodus parvus* zone in phase 2). This SST change pattern is also recorded in the Daijiagou and Liangfengya sections in South China (*35*) and is

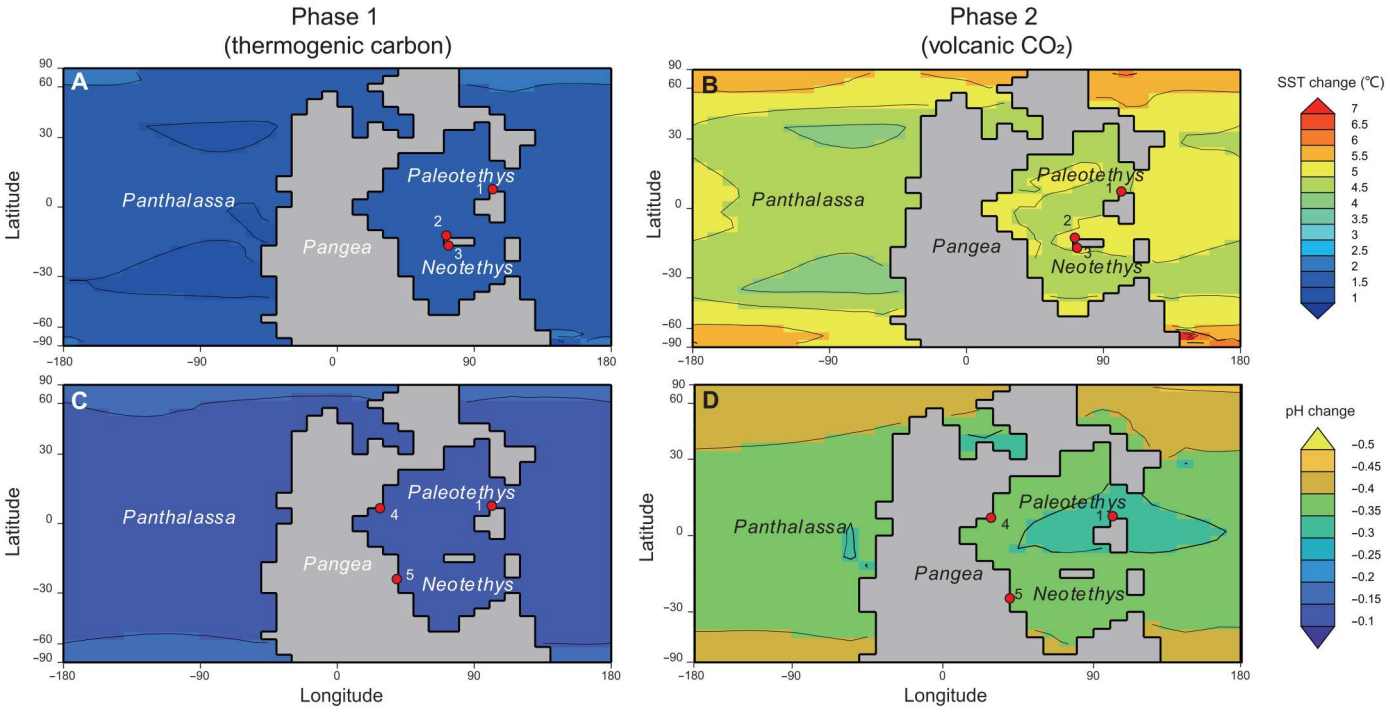


**Fig. 3. Spatial pattern of modeled global SST and pH changes during the EPME.** (**A** and **C**) SST and pH changes associated with mainly thermogenic $CO_2$ during phase 1 (251.942 Ma versus 252.02 Ma). This shows an average SST increase of 1° to 2°C and a pH decrease of 0.1- to 0.2-unit during phase 1. (**B** and **D**) SST and pH changes linked to volcanic $CO_2$-dominated emissions during phase 2 (251.902 Ma versus 251.942 Ma). A 4° to 7°C increase in SST and a 0.3- to 0.5-unit decrease in pH are shown. These model results are from the preferred experiment with median $CO_2$ scenario (experiment 2 in table S1). The absolute values of proxy-based estimates of SST and pH across the study interval are listed in table S4. The numbers in the map indicate locations of these proxy data: 1, South China; 2, Armenia; 3, Iran; 4, Italy; 5, United Arab Emirates.

more apparent than in Iran (*36*, *37*) and Armenia (*4*) (average ΔSST = 1.2°C during phase 1 and average ΔSST = 7.6°C during phase 2 based on compiled temperature proxy records shown in table S4 and Fig. 4). Our preferred model scenario shows similar degree of warming with 1° to 2°C and 4° to 7°C temperature increase during the two phases, respectively (Figs. 2D and 3), suggesting that the warming in phase 2 is associated with much increased emissions due to the evolving degassing styles associated with the Siberian Traps LIP. Our simulated decline in mean surface ocean pH also matches the proxy pH records estimated from boron isotopes of brachiopod shells from southern Alps and South China that show a 0.2- and 0.6-unit pH decrease during the

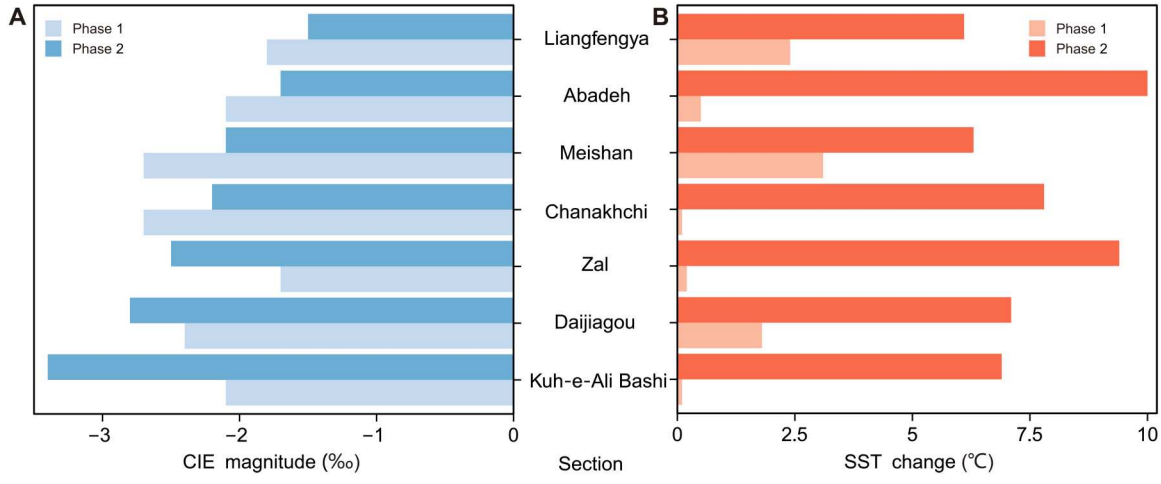


**Fig. 4. Magnitudes of $\delta^{13}C_{carb}$ excursion and proxy estimates of SST changes during the EPME.** (**A**) CIE magnitudes of $\delta^{13}C_{carb}$ during phase 1 are similar to those during phase 2. (**B**) SST changes estimated based on conodont oxygen isotopes during phase 1 are substantially smaller than those during phase 2. Details of the seven sections shown here are listed in table S4 (Meishan, Liangfengya, and Daijiagou sections are from South China; Chanakhchi section is from Armenia; and Kuh-e-Ali Bashi, Zal, and Abadeh sections are from Iran).

two phases (*13*), although the decline of pH estimated from carbonate $\delta^{11}B$ occurred at the earliest Triassic (*12*), which slightly postdates the decrease in brachiopod $\delta^{11}B$ (*13*) as well as in our model. Overall, proxy evidence supports the modeling results that the primary SST and pH change occurred during phase 2 with a smaller change during phase 1. Despite the fact that the CIE magnitudes are similar during the two phases (Fig. 4A and table S4), the primary SST increase did not occur until phase 2 (Fig. 2 and 4B), which is accounted for in our model as a change in degassing style change from small and slow thermogenic carbon emissions during phase 1, driving a small increase in SST and a large decrease in $\delta^{13}C_{carb}$, followed by rapid volcanic $CO_2$ emissions coincident with the main global warming during phase 2. That $^{206}Pb/^{238}U$ dates indicate a sequence of intrusive (251.907 ± 0.067 Ma) then extrusive (251.901 ± 0.061 Ma) magmatism (*38*) occurring during the study interval further supports our modeled degassing style change. Our modeling results are hence consistent with previous suggestions that volcanic $CO_2$ may have been the trigger for the environmental changes that occurred during the main extinction phase of the EPME (*18*).

Carbon cycle feedbacks from terrestrial ecosystem disturbances, not accounted for explicitly here, may have additionally contributed to the warming and the severity of marine extinctions. High-resolution radiometric dating and chemostratigraphy from terrestrial basins of different latitudes suggest that terrestrial ecological disturbance may have started before the main marine extinction by about 60 to 370 ka (*39*–*42*). Several plant species appear to have disappeared earlier than marine extinction, for example, records of *Gigantopteris* flora from tropical southwestern China, *Glossopteris* flora in southern high-latitude Sydney Basin, and conifer flora in mid-latitude north China were gone before the main marine extinction phase [(*39*, *43*, *44*); figs. S5 and S6]. The collapse of terrestrial ecosystem likely facilitated the oxidation of soil organic carbon and released additional $^{13}C$-depleted carbon that contributed to the low $\delta^{13}C$ value of our diagnosed carbon release during phase 1 (*34*). Furthermore, the cessation of terrestrial carbon burial that resulted from the destruction of terrestrial ecosystem (*45*) may have further amplified the warming and the severity of marine extinctions during phase 2.

### Cumulative carbon emissions across the EPME

Our best estimate for the total carbon release associated with the CIE is 26,000 (15,500 to 55,700) Pg C (Fig. 2C and table S1). This is larger than previous work based on carbon isotope mass balance calculation alone [3900 to 12,000 Pg C, (*9*)], box models (3200 to 21,600 Pg C; table S3) (*12*, *13*, *20*, *23*, *24*, *33*), or single constraint ($\delta^{13}C$) model inversion [7000 to 22,400 Pg C, (*17*); 36,200 Pg C, (*18*)]. This is despite the fact that the CIE magnitude used in this study (3.3‰) is generally smaller than those used in previous work, such as the ~5‰ CIE magnitude recorded by marine algae (*18*). Differences in the carbon isotope record used in the previous studies cannot then explain the larger cumulative $CO_2$ release that we diagnose. One factor is that the higher average $\delta^{13}C_{source}$ value (−13‰) deduced in our data assimilation requires more carbon to drive a given magnitude of CIE than those used in some prior work, in which $\delta^{13}C_{source}$ is assumed to be lower to reconcile the modeled $\delta^{13}C_{carb}$ with proxy $\delta^{13}C_{carb}$ [e.g. −25‰ in Payne and Kump (*23*)]. Furthermore, processes that remove $CO_2$ from the ocean-atmosphere system, for example, temperature-dependent silicate weathering (*46*, *47*), are not necessarily included in all of the previous studies [e.g., (*33*)]. As a modeling study by Gutjahr *et al.* (*25*) showed, $CO_2$ consumption by silicate weathering does not come to dominate the carbon budget over the main CIE, and accounting for silicate weathering would result in a slightly larger $CO_2$ release, but that the age model, CIE magnitude, and assumed source are more important. For example, we reconstructed a somewhat longer CIE duration in our study (~90 ka) as compared, for example, to Cui *et al.* (*18*) (~40 ka), which leads to the larger cumulative $CO_2$ emission inferred here. The longer CIE duration is a result of stacking marine carbonate $\delta^{13}C$ from 69 global sites based on conodont biostratigraphy and $^{206}Pb/^{238}U$ dating rather than astrochronology from a single site (*18*). A shorter CIE duration [e.g., ~40 ka as in (*18*)] would have led to a smaller total amount of $CO_2$ (12,000 to 41,200 Pg C with a median of 23,900 Pg C; sensitivity experiments 4 to 6 in table S1). That said, our estimated 26,000 (15,500 to 55,700) Pg C release is likely still an underestimate for the event as a whole because we consider only the CIE with a ~90-ka duration equivalent to the early phase of the intrusive magmatism, one of the three distinct emplacement phases of Siberian Traps LIP, across the full CIE across the Permian-Triassic transition (*15*). If the full CIE duration of ~500 ka (*29*) were considered, then more $^{13}C$-depleted $CO_2$ from contact metamorphism in the earliest Triassic is necessary (*15*). This is supported by a recent study by Jurikova *et al.* (*13*) who estimated cumulative carbon emission up to 105,600 Pg C based on a biogeochemical box model with a total emission duration of ~1 Ma.

The considerable prevailing uncertainties in the details of the time scale of the end-Permian CIE directly translate into uncertainties in diagnosed carbon emission rates. For instance, a shorter CIE duration would require a higher emission rate (fig. S2 and table S1) and make the end-Permian event more severe in terms of global carbon cycle perturbations. From our data assimilation, the carbon emission rate across the EPME (Fig. 2B) is on the same order of magnitude as that from the Paleocene-Eocene Thermal Maximum (PETM) [0.58 Pg C $year^{-1}$ in (*25*), 1.7 Pg C $year^{-1}$ in (*48*), and 0.6 to 1.1 Pg C $year^{-1}$ in (*49*)]. Notably, however, the largest mass extinction in the Phanerozoic occurred at the end-Permian (*50*), whereas the PETM was only accompanied by a minor extinction among benthic foraminifera (*51*). One explanation for this disparity is that the longer emission duration at the EPME likely produced a greater cumulative amount of carbon and caused a higher temperature rise and extinction rate (*52*, *53*) as compared to a cumulative release of 10,200 to 12,200 Pg C during the PETM (*25*, *48*, *49*). Another important factor is an increase in the strength of stabilizing feedbacks within the climate system by the time of the PETM (*54*), as evidenced by decreased extinction rates and smaller amplitude of carbon cycle perturbations through the Phanerozoic (*55*–*58*). Deep-sea carbonate production through the diversification of planktonic foraminifera and coccolithophorid algae since the Late Triassic would have greatly increased the buffering capability against changes in the carbonate chemistry and stabilized the Earth's biogeochemical cycle and climate (*59*–*61*). However, the carbon emissions that we diagnose associated with the EPME do have in common with estimates for the PETM [e.g., (*25*)] that they occur at a rate an order of magnitude slower than those associated with modern fossil fuel consumption [~10 Pg C $year^{-1}$ (*62*)]. Hence, it is likely that the anthropogenic carbon emission rate is unprecedented not only in

the past 66 Ma years (*49*) but also in the past 252 Ma years [and perhaps even 542 Ma years (*63*, *64*)].

## MATERIALS AND METHODS

### Earth system modeling

We use the "cGENIE" Earth system model of intermediate complexity, comprising a three-dimensional (3D) dynamic ocean circulation model with a 2D energy and moisture balance model of the atmosphere and a dynamic thermodynamic sea-ice model (*65*), a representation of the biogeochemical cycling of elements and isotopes (e.g. carbon, phosphorus, sulfur, and oxygen) in the ocean (*46*), plus marine sediments (*66*) and terrestrial weathering (*47*) to close the geological cycle of carbon. Two different kinds of inversion experiment can be used to solve for the geological carbon emissions with the cGENIE model. The first method inverts a $\delta^{13}C$ record to calculate the time-varying rate of carbon emissions (*18*, *67*, *68*) but requires the assumed carbon isotopes of added carbon source ($\delta^{13}C_{source}$) (as in most carbon cycle box models). The second method, called a double-inversion experiment, requires paired $\delta^{13}C$ of atmospheric $CO_2$ (or surface DIC $\delta^{13}C$) and $P_{CO_2}$ (or ocean pH), which are used to solve for both time-varying $\delta^{13}C_{source}$ and rate of carbon emissions (*25*, *26*). The later approach was adopted in the present study to achieve unique solution of $\delta^{13}C_{source}$.

cGENIE was configured on a 36 × 36 grid with 16 vertical levels in the ocean and adopted Late Permian boundary conditions of paleobathymetry and continental configuration, wind stress, and wind speed from (*69*). These boundary conditions are the same as in another recent modeling work (table S5) (*18*). The $\delta^{13}C$ value of Late Permian atmospheric $CO_2$ ($\delta^{13}C_{CO2}$) is set as −5.6‰ following (*9*). Late Permian $P_{CO_2}$ is set as ~425 ppmv based on reconstructions from stomatal proxies using fossil conifers from the Dalong Formation in South China (*70*), because these stomatal estimates have good age control (*Clarkina changxingensis* conodont zone) and reliable taxonomy and calculation method; thus, they are considered reliable. A smaller albedo is set in the model ($\alpha_{Late\ Permian} = 0.2$) compared to the present value ($\alpha_{present} = 0.3$), because climate simulations show that a single continent configuration such as the supercontinent Pangea has smaller planetary albedo than two smaller continents (*71*).

Methodologically, cGENIE was first spun up for 20 ka in a "closed system" under which there is no gain or loss of tracers from weathering or sedimentation. The steady-state climate and ocean circulation were characterized with sea-ice free poles, consistent with geological data showing no evidence of ice presence in the polar regions during the Late Permian (*3*, *72*). During a second spin-up of 400 ka, the model was run as an "open system" such that volcanic outgassing, weathering, and carbonate burial in marine sediments could reach equilibrium (with neritic $CaCO_3$ precipitation rates adjusted to balance weathering).

We then ran a series of so-called double-inversion experiments (*25*) in which cGENIE continually adjusts the rate and $\delta^{13}C$ value of emitted $CO_2$ into the atmosphere to simultaneously reproduce two proxy records as a function of time (Supplementary Materials). We use $\delta^{13}C$ of atmospheric $CO_2$ ($\delta^{13}C_{CO2}$) and $P_{CO_2}$ as the two data assimilation constraints. The $\delta^{13}C_{CO2}$ forcing is based on LOESS fit of a global $\delta^{13}C_{carb}$ dataset compiled from 10 globally distributed high–temporal resolution $\delta^{13}C_{carb}$ profiles based on a well-constrained conodont biostratigraphy (*9*), assuming that the fractionation between the atmosphere and sedimentary carbonate is −8.6‰ (*73*). The CIE magnitude of the LOESS fit $\delta^{13}C_{carb}$ record is ~3.3‰ and is considered to be globally representative, because this value is similar to the median CIE magnitude of 3.8‰ based on a $\delta^{13}C_{carb}$ compilation from 69 sites globally (*9*). The $P_{CO_2}$ profile comes from previous published data that are calculated on the basis of high-resolution $\delta^{13}C$ records of $C_3$ land plant remains from terrestrial sections in southwestern China (*9*). Experiments were run for a total duration of 180 ka—from 252.02 to 251.84 Ma and spanning the CIE. In our analysis, we focus on a ~92-ka interval from 251.994 to 251.902 Ma.

A number of sensitivity analyses were also performed to explore the effects of uncertainties in $P_{CO_2}$, CIE magnitudes, CIE durations, and $CO_2$ versus $\delta^{13}C$ age alignment scenarios. The sensitivity tests include three $CO_2$ scenarios (low, median, and high $CO_2$ scenarios) that come from the 16th percentiles, median, and 84th percentiles of the near-continuous $P_{CO_2}$ records estimated from $C_3$ land plant $CO_2$ proxy. $P_{CO_2}$ increased from 426 (330 to 559) ppmv in the latest Permian to 2507 (1314 to 7271) ppmv near the Permian-Triassic boundary (*8*), which spans the wide range of $P_{CO_2}$ estimates from other proxies, such as stomata index, paleosol carbonates, and phytane-based proxy, which vary substantially with large uncertainties (*10*, *11*, *30*, *31*, *74*, *75*). For example, the stomata-based estimates are associated with relatively low $CO_2$ levels in the latest Permian (400 to 800 ppmv) (*70*), whereas paleosol carbonates and phytane proxies show higher $CO_2$ levels (400 to 1300 ppmv) (*10*, *11*, *30*). Meanwhile, the $P_{CO_2}$ estimates in the earliest Triassic also vary notably from ~600 to ~7000 ppmv (*10*, *11*, *30*, *31*, *74*, *75*). To assess the effect of uncertainties in CIE magnitude, two larger CIE magnitudes were considered (4 and 5‰). In addition, we tested two alternative CIE durations (46 and 9.2 ka), following recent suggestions (*76*) that the CIE duration could be shorter than that used in our study (*29*). Furthermore, $^{206}Pb/^{238}U$ age and associated uncertainties suggest that the dating uncertainty is between 31 and 37 ka (*29*). This dating uncertainty may have influenced the alignment between the minimum $\delta^{13}C_{carb}$ and peak $P_{CO_2}$. Additional sensitivity analyses were performed to assess how changes in the alignment of maximum $P_{CO_2}$ and minimum $\delta^{13}C_{carb}$ affect the $CO_2$ emission pattern. These sensitivity analyses were detailed in the Supplementary Materials.

### Proxy data compilation

The reconstructed SST and pH with their paired carbon isotopes are summarized in table S4 for model-data comparison. SST determined from oxygen isotopes of conodont fossils are from three low-latitude regions of the Paleo-Tethys including the GSSP Meishan (*1*, *3*), Liangfengya and Daijiagou sections of South China (*35*), Kuh-e-Ali Bashi, Zal, and Abadeh sections of Iran (*36*, *37*), and the Chanakhchi section of Armenia (*4*). Conodont oxygen isotopes from Joachimski *et al.* (*1*) are corrected by −0.9‰ to account for the different $\delta^{18}O$ value of NBS120c standard (*4*). The equation used to calculate the SSTs is from (*77*), assuming that the sea water $\delta^{18}O$ is −1.0‰. Surface ocean pH records determined from $\delta^{11}B$ are from Dolomites of North Italy and South China (*13*) and Wadi Bih of United Arab Emirates (*12*). $\delta^{13}C$ values of marine carbonates used to calculate the CIE magnitudes come from the following sources: Meishan (*29*, *78*), Liangfengya (*79*), Daijiagou (*80*), Kuh-e-Ali Bashi (*36*), Zal (*36*), Abadeh (*81*),

Chanakhchi (*4*), Dolomites of North Italy (*13*), and Wadi Bih (*12*), and further details can be found in data file S2.

## Supplementary Materials

**This PDF file includes:**
Supplementary Text
Figs. S1 to S6
Tables S1 to S5
Legends for data S1 and S2
References

**Other Supplementary Material for this manuscript includes the following:**
Data S1 and S2

## REFERENCES AND NOTES


1. M. M. Joachimski, X. Lai, S. Shen, H. Jiang, G. Luo, B. Chen, J. Chen, Y. Sun, Climate warming in the latest Permian and the Permian–Triassic mass extinction. *Geology* **40**, 195–198 (2012).
2. Y. Sun, M. M. Joachimski, P. B. Wignall, C. Yan, Y. Chen, H. Jiang, L. Wang, X. Lai, Lethally hot temperatures during the early Triassic greenhouse. *Science* **338**, 366–370 (2012).
3. B. Chen, M. M. Joachimski, S. Z. Shen, L. L. Lambert, X. L. Lai, X. D. Wang, J. Chen, D. X. Yuan, Permian ice volume and palaeoclimate history: Oxygen isotope proxies revisited. *Gondw. Res.* **24**, 77–89 (2013).
4. M. Joachimski, A. Alekseev, A. Grigoryan, Y. A. Gatovsky, Siberian trap volcanism, global warming and the Permian-Triassic mass extinction: New insights from Armenian Permian-Triassic sections. *GSA Bull.* **132**, 427–443 (2020).
5. Y. Cui, L. R. Kump, Global warming and the end-Permian extinction event: Proxy and modeling perspectives. *Earth Sci. Rev.* **149**, 5–22 (2015).
6. W.-Q. Wang, C. Garbelli, F. F. Zhang, Q. F. Zheng, Y. C. Zhang, D. X. Yuan, Y. K. Shi, B. Chen, S. Z. Shen, A high-resolution Middle to Late Permian paleotemperature curve reconstructed using oxygen isotopes of well-preserved brachiopod shells. *Earth Planet. Sci. Lett.* **540**, 116245 (2020).
7. C. Korte, H. W. Kozur, Carbon-isotope stratigraphy across the Permian-Triassic boundary: A review. *J. Asian Earth Sci.* **39**, 215–235 (2010).
8. S.-Z. Shen, J. L. Crowley, Y. Wang, S. A. Bowring, D. H. Erwin, P. M. Sadler, C. Q. Cao, D. H. Rothman, C. M. Henderson, J. Ramezani, H. Zhang, Y. Shen, X. D. Wang, W. Wang, L. Mu, W. Z. Li, Y. G. Tang, X. L. Liu, L. J. Liu, Y. Zeng, Y. F. Jiang, Y. G. Jin, Calibrating the end-Permian mass extinction. *Science* **334**, 1367–1372 (2011).
9. Y. Wu, D. Chu, J. Tong, H. Song, J. D. Corso, P. B. Wignall, H. Song, Y. Du, Y. Cui, Six-fold increase of atmospheric $pCO_2$ during the Permian–Triassic mass extinction. *Nat. Commun.* **12**, 1–8 (2021).
10. M. M. Joachimski, J. Müller, T. M. Gallagher, G. Mathes, D. L. Chu, F. Mouraviev, V. Silantiev, Y. D. Sun, J. N. Tong, Five million years of high atmospheric $CO_2$ in the aftermath of the Permian-Triassic mass extinction. *Geology* **50**, 650–654 (2022).
11. J. Shen, Y. G. Zhang, H. Yang, S. Xie, A. Pearson, Early and late phases of the Permian–-Triassic mass extinction marked by different atmospheric $CO_2$ regimes. *Nat. Geosci.* **15**, 839–844 (2022).
12. M. O. Clarkson, S. A. Kasemann, R. A. Wood, T. M. Lenton, S. J. Daines, S. Richoz, F. Ohnemueller, A. Meixner, S. W. Poulton, E. T. Tipper, Ocean acidification and the Permo-Triassic mass extinction. *Science* **348**, 229–232 (2015).
13. H. Jurikova, M. Gutjahr, K. Wallmann, S. Flögel, V. Liebetrau, R. Posenato, L. Angiolini, C. Garbelli, U. Brand, M. Wiedenbeck, A. Eisenhauer, Permian–Triassic mass extinction pulses driven by major marine carbon cycle perturbations. *Nat. Geosci.* **13**, 745–750 (2020).
14. H. Svensen, S. Planke, A. G. Polozov, N. Schmidbauer, F. Corfu, Y. Y. Podladchikov, B. Jamtveit, Siberian gas venting and the end-Permian environmental crisis. *Earth Planet. Sci. Lett.* **277**, 490–500 (2009).
15. S. Burgess, J. Muirhead, S. Bowring, Initial pulse of Siberian Traps sills as the trigger of the end-Permian mass extinction. *Nat. Commun.* **8**, 164 (2017).
16. H. Zhang, F. Zhang, J.-B. Chen, D. H. Erwin, D. D. Syverson, P. Ni, M. Rampino, Z. Chi, Y.-F. Cai, L. Xiang, W.-Q. Li, S.-A. Liu, R.-C. Wang, X.-D. Wang, Z. Feng, H.-M. Li, T. Zhang, H.-M. Cai, W. Zheng, Y. Cui, X.-K. Zhu, Z.-Q. Hou, F.-Y. Wu, Y.-G. Xu, N. Planavsky, S.-Z. Shen, Felsic volcanism as a factor driving the end-Permian mass extinction. *Sci. Adv.* **7**, eabh1390 (2021).
17. Y. Cui, L. R. Kump, A. Ridgwell, Initial assessment of the carbon emission rate and climatic consequences during the end-Permian mass extinction. *Palaeogeogr. Palaeoclimatol. Palaeoecol.* **389**, 128–136 (2013).
18. Y. Cui, M. Li, E. E. van Soelen, F. Peterse, W. M. Kürschner, Massive and rapid predominantly volcanic $CO_2$ emission during the end-Permian mass extinction. *Proc. Natl. Acad. Sci. U.S.A.* **118**, e2014701118 (2021).
19. J. E. Tierney, C. J. Poulsen, I. P. Montañez, T. Bhattacharya, R. Feng, H. L. Ford, B. Hönisch, G. N. Inglis, S. V. Petersen, N. Sagoo, C. R. Tabor, K. Thirumalai, J. Zhu, N. J. Burls, G. L. Foster, Y. Goddéris, B. T. Huber, L. C. Ivany, S. K. Turner, D. J. Lunt, J. C. McElwain, B. J. W. Mills, B. L. Otto-Bliesner, A. Ridgwell, Y. G. Zhang, Past climates inform our future. *Science* **370**, eaay3701 (2020).
20. R. A. Berner, Examination of hypotheses for the Permo–Triassic boundary extinction by carbon cycle modeling. *Proc. Natl. Acad. Sci. U.S.A.* **99**, 4172–4177 (2002).
21. A. Grard, L. Francois, C. Dessert, B. Dupré, Y. Godderis, Basaltic volcanism and mass extinction at the Permo-Triassic boundary: Environmental impact and modeling of the global carbon cycle. *Earth Planet. Sci. Lett.* **234**, 207–221 (2005).
22. M. R. Rampino, K. Caldeira, Major perturbation of ocean chemistry and a 'Strangelove Ocean' after the end-Permian mass extinction. *Terra Nova* **17**, 554–559 (2005).
23. J. Payne, L. Kump, Evidence for recurrent Early Triassic massive volcanism from quantitative interpretation of carbon isotope fluctuations. *Earth Planet. Sci. Lett.* **256**, 264–277 (2007).
24. N. Komar, R. Zeebe, Calcium and calcium isotope changes during carbon cycle perturbations at the end-Permian. *Paleoceanography* **31**, 115–130 (2016).
25. M. Gutjahr, A. Ridgwell, P. F. Sexton, E. Anagnostou, P. N. Pearson, H. Pälike, R. D. Norris, E. Thomas, G. L. Foster, Very large release of mostly volcanic carbon during the Palaeocene–Eocene thermal maximum. *Nature* **548**, 573–577 (2017).
26. M. Adloff, S. E. Greene, I. J. Parkinson, B. D. A. Naafs, W. Preston, A. Ridgwell, D. J. Lunt, J. M. Castro Jiménez, F. M. Monteiro, Unravelling the sources of carbon emissions at the onset of Oceanic Anoxic Event (OAE) 1a. *Earth Planet. Sci. Lett.* **530**, 115947 (2020).
27. H. Yin, H. Jiang, W. Xia, Q. Feng, N. Zhang, J. Shen, The end-Permian regression in South China and its implication on mass extinction. *Earth Sci. Rev.* **137**, 19–33 (2014).
28. D.-X. Yuan, S. Shen, C. Henderson, J. Chen, H. Zhang, H.-Z. Feng, Revised conodont-based integrated high-resolution timescale for the Changhsingian stage and end-Permian extinction interval at the Meishan sections, South China. *Lithos* **204**, 220–245 (2014).
29. S. D. Burgess, S. Bowring, S.-Z. Shen, High-precision timeline for Earth's most severe extinction. *Proc. Natl. Acad. Sci. U.S.A.* **111**, 3316–3321 (2014).
30. C. R. Witkowski, J. W. H. Weijers, B. Blais, S. Schouten, J. S. Sinninghe Damsté, Molecular fossils from phytoplankton reveal secular $pCO_2$ trend over the Phanerozoic. *Sci. Adv.* **4**, eaat4556 (2018).
31. G. J. Retallack, Multiple Permian-Triassic life crises on land and at sea. *Global Planet. Change* **198**, 103415 (2021).
32. J. Frieling, F. Peterse, D. J. Lunt, S. M. Bohaty, J. S. Sinninghe Damsté, G. J. Reichart, A. Sluijs, Widespread warming before and elevated barium burial during the paleocene-eocene thermal maximum: Evidence for methane hydrate release? *Paleoceanogr. Paleoclimatol.* **34**, 546–566 (2019).
33. J. L. Payne, A. V. Turchyn, A. Paytan, D. J. DePaolo, D. J. Lehrmann, M. Yu, J. Wei, Calcium isotope constraints on the end-Permian mass extinction. *Proc. Natl. Acad. Sci. U.S.A.* **107**, 8543–8548 (2010).
34. J. Dal Corso, B. J. W. Mills, D. Chu, R. J. Newton, T. A. Mather, W. Shu, Y. Wu, J. Tong, P. B. Wignall, Permo–Triassic boundary carbon and mercury cycling linked to terrestrial ecosystem collapse. *Nat. Commun.* **11**, 2962 (2020).
35. J. Chen, S. Z. Shen, X. H. Li, Y. G. Xu, M. M. Joachimski, S. A. Bowring, D. H. Erwin, D. X. Yuan, B. Chen, H. Zhang, Y. Wang, C. Q. Cao, Q. F. Zheng, L. Mu, High-resolution SIMS oxygen isotope analysis on conodont apatite from South China and implications for the end-Permian mass extinction. *Palaeogeogr. Palaeoclimatol. Palaeoecol.* **448**, 26–38 (2016).
36. M. Schobben, M. M. Joachimski, D. Korn, L. Leda, C. Korte, Palaeotethys seawater temperature rise and an intensified hydrological cycle following the end-Permian mass extinction. *Gondw. Res.* **26**, 675–683 (2014).
37. J. Chen, S. Z. Shen, Y. C. Zhang, L. Angiolini, M. N. Gorgij, G. Crippa, W. Wang, H. Zhang, D. X. Yuan, X. H. Li, Y. G. Xu, Abrupt warming in the latest Permian detected using high-resolution in situ oxygen isotopes of conodont apatite from Abadeh, central Iran. *Palaeogeogr. Palaeoclimatol. Palaeoecol.* **560**,109973(2020).
38. S. D. Burgess, S. A. Bowring, High-precision geochronology confirms voluminous magmatism before, during, and after Earth's most severe extinction. *Sci. Adv.* **1**, e1500470 (2015).
39. D. Chu, S. E. Grasby, H. Song, J. D. Corso, Y. Wang, T. A. Mather, Y. Wu, H. Song, W. Shu, J. Tong, P. B. Wignall, Ecological disturbance in tropical peatlands prior to marine Permian-Triassic mass extinction. *Geology* **48**, 288–292 (2020).
40. C. R. Fielding, T. D. Frank, S. McLoughlin, V. Vajda, C. Mays, A. P. Tevyaw, A. Winguth, C. Winguth, R. S. Nicoll, M. Bocking, J. L. Crowley, Age and pattern of the southern high-

latitude continental end-Permian extinction constrained by multiproxy analysis. *Nat. Commun.* **10**, 385 (2019).
41. R. A. Gastaldo, S. L. Kamo, J. Neveling, J. W. Geissman, C. V. Looy, A. M. Martini, The base of the Lystrosaurus Assemblage Zone, Karoo Basin, predates the end-Permian marine extinction. *Nat. Commun.* **11**, 1–8 (2020).
42. J. Dal Corso, H. Song, S. Callegaro, D. Chu, Y. Sun, J. Hilton, S. E. Grasby, M. M. Joachimski, P. B. Wignall, Environmental crises at the Permian–Triassic mass extinction. *Nat. Rev. Earth Environ.* **3**, 197–214 (2022).
43. T. D. Frank, C. R. Fielding, A. M. E. Winguth, K. Savatic, A. Tevyaw, C. Winguth, S. McLoughlin, V. Vajda, C. Mays, R. Nicoll, M. Bocking, J. L. Crowley, Pace, magnitude, and nature of terrestrial climate change through the end-Permian extinction in southeastern Gondwana. *Geology* **49**, 1089–1095 (2021).
44. Y. Wu, J. Tong, T. J. Algeo, D. Chu, Y. Cui, H. Song, W. Shu, Y. du, Organic carbon isotopes in terrestrial Permian-Triassic boundary sections of North China: Implications for global carbon cycle perturbations. *GSA Bull.* **132**, 1106–1118 (2020).
45. V. Vajda, S. McLoughlin, C. Mays, T. D. Frank, C. R. Fielding, A. Tevyaw, V. Lehsten, M. Bocking, R. S. Nicoll, End-Permian (252 Mya) deforestation, wildfires and flooding—An ancient biotic crisis with lessons for the present. *Earth Planet. Sci. Lett.* **529**, 115875 (2020).
46. A. Ridgwell, J. C. Hargreaves, N. R. Edwards, J. D. Annan, T. M. Lenton, R. Marsh, A. Yool, A. Watson, Marine geochemical data assimilation in an efficient Earth System Model of global biogeochemical cycling. *Biogeosciences* **4**, 87–104 (2007).
47. G. Colbourn, A. Ridgwell, T. M. Lenton, The Rock Geochemical Model (RokGeM) v0.9. *Geosci. Model Dev.* **6**, 1543–1573 (2013).
48. Y. Cui, L. R. Kump, A. J. Ridgwell, A. J. Charles, C. K. Junium, A. F. Diefendorf, K. H. Freeman, N. M. Urban, I. C. Harding, Slow release of fossil carbon during the Palaeocene-Eocene Thermal Maximum. *Nat. Geosci.* **4**, 481–485 (2011).
49. R. E. Zeebe, A. Ridgwell, J. C. Zachos, Anthropogenic carbon release rate unprecedented during the past 66 million years. *Nat. Geosci.* **9**, 325–329 (2016).
50. J.-X. Fan, S. Z. Shen, D. H. Erwin, P. M. Sadler, N. MacLeod, Q. M. Cheng, X. D. Hou, J. Yang, X. D. Wang, Y. Wang, H. Zhang, X. Chen, G. X. Li, Y. C. Zhang, Y. K. Shi, D. X. Yuan, Q. Chen, L. N. Zhang, C. Li, Y. Y. Zhao, A high-resolution summary of Cambrian to Early Triassic marine invertebrate biodiversity. *Science* **367**, 272–277 (2020).
51. E. Thomas, in *Late Paleocene-Early Eocene Climatic and Biotic Events in the Marine and Terrestrial Records*, M.-P. Aubry, S. G. Lucas, W. A. Berggren, Eds. (Columbia University Press, 1998).
52. H. Song, D. B. Kemp, L. Tian, D. Chu, H. Song, X. Dai, Thresholds of temperature change for mass extinctions. *Nat. Commun.* **12**, 4694 (2021).
53. D. P. Bond, S. E. Grasby, On the causes of mass extinctions. *Palaeogeogr. Palaeoclimatol. Palaeoecol.* **478**, 3–29 (2017).
54. D. E. Penman, Silicate weathering and North Atlantic silica burial during the Paleocene-Eocene Thermal Maximum. *Geology* **44**, 731–734 (2016).
55. J. L. Payne, A. Bachan, N. A. Heim, P. M. Hull, M. L. Knope, The evolution of complex life and the stabilization of the Earth system. *Interface Focus* **10**, 20190106 (2020).
56. A. Bachan, K. V. Lau, M. R. Saltzman, E. Thomas, L. R. Kump, J. L. Payne, A model for the decrease in amplitude of carbon isotope excursions across the Phanerozoic. *Am. J. Sci.* **317**, 641–676 (2017).
57. R. G. Stockey, A. Pohl, A. Ridgwell, S. Finnegan, E. A. Sperling, Decreasing Phanerozoic extinction intensity as a consequence of Earth surface oxygenation and metazoan ecophysiology. *Proc. Natl. Acad. Sci. U.S.A.* **118**, e2101900118 (2021).
58. J. Alroy, Accurate and precise estimates of origination and extinction rates. *Paleobiology* **40**, 374–397 (2014).
59. A. Ridgwell, A Mid Mesozoic Revolution in the regulation of ocean chemistry. *Mar. Geol.* **217**, 339–357 (2005).
60. A. H. Knoll, M. J. Follows, A bottom-up perspective on ecosystem change in Mesozoic oceans. *Proc. R. Soc. B.* **283**, 20161755 (2016).
61. K. Eichenseer, U. Balthasar, C. W. Smart, J. Stander, K. A. Haaga, W. Kiessling, Jurassic shift from abiotic to biotic control on marine ecological success. *Nat. Geosci.* **12**, 638–642 (2019).
62. P. Friedlingstein, M. O'Sullivan, M. W. Jones, R. M. Andrew, J. Hauck, A. Olsen, G. P. Peters, W. Peters, J. Pongratz, S. Sitch, C. le Quéré, J. G. Canadell, P. Ciais, R. B. Jackson, S. Alin, L. E. O. C. Aragão, A. Arneth, V. Arora, N. R. Bates, M. Becker, A. Benoit-Cattin, H. C. Bittig, L. Bopp, S. Bultan, N. Chandra, F. Chevallier, L. P. Chini, W. Evans, L. Florentie, P. M. Forster, T. Gasser, M. Gehlen, D. Gilfillan, T. Gkritzalis, L. Gregor, N. Gruber, I. Harris, K. Hartung, V. Haverd, R. A. Houghton, T. Ilyina, A. K. Jain, E. Joetzjer, K. Kadono, E. Kato, V. Kitidis, J. I. Korsbakken, P. Landschützer, N. Lefèvre, A. Lenton, S. Lienert, Z. Liu, D. Lombardozzi, G. Marland, N. Metzl, D. R. Munro, J. E. M. S. Nabel, S. I. Nakaoka, Y. Niwa, K. O'Brien, T. Ono, P. I. Palmer, D. Pierrot, B. Poulter, L. Resplandy, E. Robertson, C. Rödenbeck, J. Schwinger, R. Séférian, I. Skjelvan, A. J. P. Smith, A. J. Sutton, T. Tanhua, P. P. Tans, H. Tian, B. Tilbrook, G. van der Werf, N. Vuichard, A. P. Walker, R. Wanninkhof, A. J. Watson, D. Willis, A. J. Wiltshire, W. Yuan, X. Yue, S. Zaehle, Global carbon budget 2020. *Earth Syst. Sci. Data* **12**, 3269–3340 (2020).
63. D. H. Rothman, Thresholds of catastrophe in the Earth system. *Sci. Adv.* **3**, e1700906 (2017).
64. D. H. Rothman, Characteristic disruptions of an excitable carbon cycle. *Proc. Natl. Acad. Sci. U.S.A.* **116**, 14813–14822 (2019).
65. N. R. Edwards, R. Marsh, Uncertainties due to transport-parameter sensitivity in an efficient 3-D ocean-climate model. *Climate Dynam.* **24**, 415–433 (2005).
66. A. Ridgwell, J. C. Hargreaves, Regulation of atmospheric $CO_2$ by deep-sea sediments in an Earth system model. *Global Biogeochem. Cycles* **21**, GB2008 (2007).
67. S. Kirtland Turner, A. Ridgwell, Development of a novel empirical framework for interpreting geological carbon isotope excursions, with implications for the rate of carbon injection across the PETM. *Earth Planet. Sci. Lett.* **435**, 1–13 (2016).
68. P. Vervoort, M. Adloff, S. Greene, S. K. Turner, Negative carbon isotope excursions: An interpretive framework. *Environ. Res. Lett.* **14**, 085014 (2019).
69. J. Kiehl, C. Shields, Climate simulation of the latest Permian: Implications for mass extinction. *Geology* **33**, 757 (2005).
70. H. Li, J. Yu, J. C. McElwain, C. Yiotis, Z.-Q. Chen, Reconstruction of atmospheric $CO_2$ concentration during the late Changhsingian based on fossil conifers from the Dalong Formation in South China. *Palaeogeogr. Palaeoclimatol. Palaeoecol.* **519**, 37–48 (2019).
71. C. R. Tabor, R. Feng, B. L. Otto-Bliesner, Climate responses to the splitting of a supercontinent: Implications for the breakup of Pangea. *Geophys. Res. Lett.* **46**, 6059–6068 (2019).
72. R. A. Gastaldo, W. A. DiMichele, H. W. Pfefferkorn, Out of the icehouse into the greenhouse: A late Paleozoic analogue for modern global vegetational change. *GSA Today* **6**, 1–7 (1996).
73. J. Zhang, P. Quay, D. Wilbur, Carbon isotope fractionation during gas-water exchange and dissolution of $CO_2$. *Geochim. Cosmochim. Acta* **59**, 107–114 (1995).
74. D. D. Ekart, T. E. Cerling, I. P. Montanez, N. J. Tabor, A 400 million year carbon isotope record of pedogenic carbonate; implications for paleoatomospheric carbon dioxide. *Am. J. Sci.* **299**, 805–827 (1999).
75. R. A. Gastaldo, C. L. Knight, J. Neveling, N. J. Tabor, Latest Permian paleosols from Wapadsberg Pass, South Africa: Implications for Changhsingian climate. *Geol. Soc. Am. Bull.* **126**, 665–679 (2014).
76. S.-Z. Shen, J. Ramezani, J. Chen, C.-Q. Cao, D. H. Erwin, H. Zhang, L. Xiang, S. D. Schoepfer, C. M. Henderson, Q.-F. Zheng, S. A. Bowring, Y. Wang, X.-H. Li, X.-D. Wang, D.-X. Yuan, Y.-C. Zhang, L. Mu, J. Wang, Y.-S. Wu, A sudden end-Permian mass extinction in South China. *GSA Bull.* **131**, 205–223 (2019).
77. E. Pucéat, M. M. Joachimski, A. Bouilloux, F. Monna, A. Bonin, S. Motreuil, P. Morinière, S. Hénard, J. Mourin, G. Dera, Revised phosphate-water fractionation equation reassessing paleotemperatures derived from biogenic apatite. *Earth Planet. Sci. Lett.* **298**, 135–142 (2010).
78. C. Cao, G. D. Love, L. E. Hays, W. Wang, S. Shen, R. E. Summons, Biogeochemical evidence for euxinic oceans and ecological disturbance presaging the end-Permian mass extinction event. *Earth Planet. Sci. Lett.* **281**, 188–201 (2009).
79. K. Kaiho, M. Aftabuzzaman, D. S. Jones, L. Tian, Pulsed volcanic combustion events coincident with the end-Permian terrestrial disturbance and the following global crisis. *Geology* **49**, 289–293 (2021).
80. D.-x. Yuan, J. Chen, Y.-c. Zhang, Q.-f. Zheng, S.-z. Shen, Changhsingian conodont succession and the end-Permian mass extinction event at the Daijiagou section in Chongqing, Southwest China. *J. Asian Earth Sci.* **105**, 234–251 (2015).
81. X.-C. Liu, W. Wang, S. Z. Shen, M. N. Gorgij, F. C. Ye, Y. C. Zhang, S. Furuyama, A. Kano, X. Z. Chen, Late Guadalupian to Lopingian (Permian) carbon and strontium isotopic chemostratigraphy in the Abadeh section, central Iran. *Gondw. Res.* **24**, 222–232 (2013).
82. T. J. Algeo, B. Ellwood, T. K. T. Nguyen, H. Rowe, J. B. Maynard, The Permian–Triassic boundary at Nhi Tao, Vietnam: Evidence for recurrent influx of sulfidic watermasses to a shallow-marine carbonate platform. *Palaeogeogr. Palaeoclimatol. Palaeoecol.* **252**, 304–327 (2007).
83. M. Schobben, C. V. Ullmann, L. Leda, D. Korn, U. Struck, W. U. Reimold, A. Ghaderi, T. J. Algeo, C. Korte, Discerning primary versus diagenetic signals in carbonate carbon and oxygen isotope records: An example from the Permian–Triassic boundary of Iran. *Chem. Geol.* **422**, 94–107 (2016).
84. M. O. Clarkson, S. Richoz, R. A. Wood, F. Maurer, L. Krystyn, D. J. GMcGurty, D. Astratti, A new high-resolution δ13C record for the Early Triassic: Insights from the Arabian Platform. *Gondw. Res.* **24**, 233–242 (2013).
85. C. Ji, Z. Wu, H. Yi, G. Xia, Z. Zhao, T. Wang, $^{13}C$-$^{18}O$ isotopic anomalous study of the carbonate rock at the Wenbudangsang PTB section,Tibet (in Chinese with English abstract). *Acta Geol. Sin.* **92**, 2018–2027 (2018).

86. H. Song, J. N. Tong, Y. L. Xiong, D. Y. Sun, L. Tian, H. Y. Song, The large increase of δ $^{13}C_{carb}$-depth gradient and the end-Permian mass extinction. *Sci. China Earth Sci.* **55**, 1101–1109 (2012).
87. T. Algeo, Y. Shen, T. Zhang, T. Lyons, S. Bates, H. Rowe, T. K. T. Nguyen, Association of $^{34}S$-depleted pyrite layers with negative carbonate $\delta^{13}C$ excursions at the Permian-Triassic boundary: Evidence for upwelling of sulfidic deep-ocean water masses. *Geochem. Geophys. Geosyst.* **9**, Q04025 (2008).
88. J. Haas, A. Demény, K. Hips, N. Zajzon, T. G. Weiszburg, M. Sudar, J. Pálfy, Biotic and environmental changes in the Permian-Triassic boundary interval recorded on a western Tethyan ramp in the Bükk Mountains, Hungary. *Glob. Planet. Change* **55**, 136–154 (2007).
89. D. P. Bond, P. B. Wignall, Pyrite framboid study of marine Permian–Triassic boundary sections: A complex anoxic event and its relationship to contemporaneous mass extinction. *Geol. Soc. Am. Bull.* **122**, 1265–1279 (2010).
90. H. W. Kozur, Biostratigraphy and event stratigraphy in Iran around the Permian-Triassic Boundary (PTB): Implications for the causes of the PTB biotic crisis. *Global Planet. Change* **55**, 155–176 (2007).
91. T. Galfetti, H. Bucher, A. Brayard, P. A. Hochuli, H. Weissert, K. Guodun, V. Atudorei, J. Guex, Late Early Triassic climate change: Insights from carbonate carbon isotopes, sedimentary evolution and ammonoid paleobiogeography. *Palaeogeogr. Palaeoclimat. Palaeoecol.* **243**, 394–411 (2007).
92. C. Korte, H. W. Kozur, P. Mohtat-Aghai, Dzulfian to lowermost Triassic $\delta^{13}C$ record at the Permian/Triassic boundary section at Shahreza, central Iran. *Hallesches Jahrbuch für Geowissenschaften, Reihe B Geologie, Paläontologie, Mineralogie* **18**, 73–38 (2004).
93. C. Korte, H. W. Kozur, M. M. Joachimski, H. Strauss, J. Veizer, L. Schwark, Carbon, sulfur, oxygen and strontium isotope records, organic geochemistry and biostratigraphy across the Permian/Triassic boundary in Abadeh Iran. *Int. J. Earth Sci.* **93**, 565–581 (2004).
94. C. Korte, P. Pande, P. Kalia, H. W. Kozur, M. M. Joachimski, H. Oberhänsli, Massive volcanism at the Permian-Triassic boundary and its impact on the isotopic composition of the ocean and atmosphere. *J. Asian Earth Sci.* **37**, 293–311 (2010).

**Acknowledgments:** We thank L. R. Kump for inspiration and insights. This paper benefited greatly from comments from two anonymous reviewers and the associate editor P. Donoghue. **Funding:** This work was supported by NSF grant EAR-2026877 (to Y.C.), National Natural Science Foundation of China grants 92155201, 42030513, 42072025, and 92255303 (to H.S., D.C., J.T., and J.D.C.) and NSF grant EAR-2121165 (to A.R.) . **Author contributions:** Conceptualization: Y.C., Y.W., and D.C. Methodology: Y.C., Y.W., and A.R. Investigation: Y.C., Y.W., and D.C. Visualization: Y.W. Supervision: Y.C. and D.C. Writing—original draft: Y.W., Y.C., and D.C. Writing—review and editing: D.C., H.S., J.T., J.D.C., and A.R. **Competing interests:** The authors declare that they have no competing interests. **Data and materials availability:** All data needed to evaluate the conclusions in the paper are present in the paper and/or the Supplementary Materials. The code for the version of the "muffin" release of the cGENIE Earth system model used here is tagged as v0.9.37 and is assigned a DOI: 10.5281/zenodo.7549086. Configuration files for the specific experiments presented in the paper can be found in the directory: genie-userconfigs/PUBS/published/Wu_et_al.2023. Details of the experiments, plus the command line needed to run each one, are given in the readme.txt file in that directory. All other configuration files and boundary conditions are provided as part of the code release. A manual detailing code installation, basic model configuration, tutorials covering various aspects of model configuration, experimental design, and output, plus the processing of results, is assigned a DOI: 10.5281/zenodo.7545814.

Submitted 13 April 2022
Accepted 18 January 2023
Published 15 February 2023
10.1126/sciadv.abq4082